

# A high-resolution time-of-flight energy analyzer for femtosecond electron pulses at 30 keV

Alexander Gliserin, Matthew Walbran, and Peter Baum

Citation: [Review of Scientific Instruments](#) **87**, 033302 (2016); doi: 10.1063/1.4942912

View online: <http://dx.doi.org/10.1063/1.4942912>

View Table of Contents: <http://aip.scitation.org/toc/rsi/87/3>

Published by the [American Institute of Physics](#)

---

## Articles you may be interested in

[Ultrafast electron crystallography of the cooperative reaction path in vanadium dioxide](#)  
*Structural Dynamics* **3**, 034304 (2016); 10.1063/1.4953370

[Time-of-flight electron energy loss spectroscopy using TM<sub>110</sub> deflection cavities](#)  
*Structural Dynamics* **3**, 054303 (2016); 10.1063/1.4962698

[Femtosecond single-electron diffraction](#)  
*Structural Dynamics* **1**, 034303 (2014); 10.1063/1.4884937

[Mega-electron-volt ultrafast electron diffraction at SLAC National Accelerator Laboratory](#)  
*Review of Scientific Instruments* **86**, 073702 (2015); 10.1063/1.4926994

[A general method for baseline-removal in ultrafast electron powder diffraction data using the dual-tree complex wavelet transform](#)  
*Structural Dynamics* **4**, 044004 (2016); 10.1063/1.4972518

[Tip-based source of femtosecond electron pulses at 30 keV](#)  
*Journal of Applied Physics* **115**, 094506 (2014); 10.1063/1.4867185

---



# A high-resolution time-of-flight energy analyzer for femtosecond electron pulses at 30 keV

Alexander Gliserin,<sup>a)</sup> Matthew Walbran, and Peter Baum<sup>a)</sup>

Ludwig-Maximilians-Universität München, Am Coulombwall 1, 85748 Garching, Germany  
and Max-Planck-Institute of Quantum Optics, Hans-Kopfermann-Str. 1, 85748 Garching, Germany

(Received 21 September 2015; accepted 13 February 2016; published online 1 March 2016)

We report a time-of-flight spectrometer for electron pulses at up to 30 keV, which is a suitable energy for atomic-resolution femtosecond investigations via time-resolved electron diffraction, microscopy, and energy loss spectroscopy. For realistic femtosecond beams without apertures, the instrument's energy resolution is  $\sim 0.5$  eV (full width at half maximum) or  $2 \times 10^{-5}$  at a throughput of 50%-90%. We demonstrate the analyzer's versatility by three first applications, namely, femtosecond electron pulse metrology via optical streaking, *in situ* drift correction in laser-microwave synchronization for electron pulse compression, and time-resolved electron energy loss spectroscopy of aluminum, showing the instrument's capability of tracking plasmonic loss peak positions with few-meV accuracy. © 2016 AIP Publishing LLC. [<http://dx.doi.org/10.1063/1.4942912>]

## I. INTRODUCTION

Electron pulses of femtosecond duration have recently enabled taking atomic-scale matter snapshots during ongoing ultrafast transformations.<sup>1-10</sup> Basically, a laser pulse triggers the reaction of interest and ultrashort electron pulses subsequently probe the reaction path while the material proceeds from an initial to a final conformation. Ideal for achieving atomic-resolution diffraction are electron energies of 10-300 keV, i.e., a de Broglie wavelength of 1-10 pm. Electron diffraction provides picometer resolution of sub-unit-cell dynamics and electron microscopy is ideal for the study of complex materials such as biological specimens or nanostructures via direct time-resolved imaging in the real-space domain. Recently, femtosecond electron energy loss spectroscopy (EELS) has emerged as an additional alternative to access the dynamics of matter transformations.<sup>11,12</sup> Here, close-to-monochromatic electron pulses are sent through the specimen after femtosecond laser excitation and the loss spectrum is recorded in dependence on the pump-probe delay. This technique can access the near-edge (meV), plasmonic (eV), and core regimes (hundreds of eV) of electron energy loss with femtosecond time resolution. This reveals some very complementary information as compared to diffraction or microscopy, namely, site-selective (e.g., core level and near-edge) or function-specific (e.g., plasmonic) effects.

A central problem with femtosecond electron diffraction and spectroscopy, however, is the limited amount of average electron current that is available. On one hand, the pump-probe repetition rate is limited by the sample's reversibility.<sup>13,14</sup> On the other hand, space charge effects<sup>15</sup> oppose condensing a large number of electrons into bright and ultrashort pulses, i.e., pulses with adequate electron density, duration, beam size, and transverse coherence at the same time.<sup>8</sup> In combination, although the linear chirp caused by space charge forces<sup>15</sup> can

to some extent be reduced via microwave compression,<sup>16,17</sup> a limited electron current at a limited beam quality remains a key restriction.

For time-resolved EELS at femtosecond resolution, this problem unfortunately renders the electron spectrometers commonly applied in transmission electron microscopes to a large extent inappropriate. At energies of tens of keV and above, energy filters such as magnetic sectors<sup>18</sup> or Wien filters<sup>19</sup> can only provide quite limited energy-dependent deflection, typically only nanometers per meV. Therefore, significant spatial filters (slits, apertures) are usually required, introducing a substantial loss in electron flux. In the case of femtosecond electron pulses, this would further reduce the very scarce number of available electrons and hence escalate the overall measurement time in many cases beyond feasibility.

Highly desirable for future investigations with femtosecond electron pulses is therefore an electron energy analyzer that is (a) suitable for central energies of tens of keV while providing (b) close to 100% detection efficiency and (c) meV resolution capability. Electrostatic analyzers in hemispherical or cylindrical configuration currently reach electron energies up to 15 keV<sup>20-23</sup> and could in principle be scaled up, but such devices are technically intricate and also large and expensive constructions. Simpler deflecting analyzers at tens of keV have also been reported,<sup>24-26</sup> but do not provide sufficient energy resolution.

In contrast to deflecting analyzers, a time-of-flight (ToF) spectrometer introduces the energy-dependent dispersion in the time domain rather than in space. This is usually achieved by letting electrons propagate through a drift tube that is electrostatically biased to increase the temporal dispersion. Measuring the arrival time of the electrons at a detector with respect to a clock reveals their velocity and thus their kinetic energy. This concept requires a pulsed electron beam, but it is naturally available in femtosecond experiments. All electron energies are measured simultaneously at the detector without the need for sweeping, avoiding any associated reduction in acquisition speed. In addition, the ToF concept provides a quite

<sup>a)</sup>Electronic addresses: alex.gliserin@lmu.de and peter.baum@lmu.de

high energy resolution for rather divergent and large beams; also the construction is relatively simple and inexpensive. This makes the ToF analyzer an ideal choice for the limited beam quality in femtosecond electron pump-probe experiments.

However, time-of-flight energy analyzer implementations for photoelectron spectroscopy<sup>27-30</sup> are limited to kinetic energies in the low keV range,<sup>31</sup> insufficient for atomic-scale diffraction. Thus, we report here a ToF spectrometer for electron pulses at up to 30 keV, a suitable energy for femtosecond diffraction.<sup>1,32</sup> The analyzer provides an energy resolution of  $<0.6$  eV (full-width at half maximum, FWHM) over a selectable range of 5 eV and a resolution of better than 3 eV (FWHM) over a range of 50 eV. This corresponds to a relative energy resolution of down to  $2 \times 10^{-5}$ . For a realistic close-to-collimated femtosecond electron beam of  $\sim 300$   $\mu\text{m}$  diameter, the transmission efficiency is better than 50% for the highest resolution range ( $<0.6$  eV FWHM) and better than 90% elsewhere. This high efficiency is achieved without the need for any aperture or slit, hence at the full electron current available from the femtosecond source.

We first describe the apparatus and its construction in detail. Next, we report on calibration procedures before characterizing the performance and its limitations. Finally, three first applications in the context of femtosecond electron science are reported: First, we perform an extensive temporal and energetic characterization of laser-generated femtosecond single-electron pulses at 25 keV via laser streaking in the time-energy domain, as reported previously in a different experiment.<sup>33</sup> Second, we apply the ToF analyzer as a diagnostics tool for microwave-based electron pulse compression; the residual long-term timing drifts of the applied laser-microwave synchronization concept<sup>34</sup> can be detected with a precision of 1 fs root mean square (rms) with only 5 s of integration time per measurement.<sup>35</sup> Third, we report on time-resolved EELS of aluminum using low-flux single-electron pulses at 5 MHz repetition rate, revealing that the center of the bulk plasmon loss peak can be determined with  $\sim 3$  meV (rms) precision at an electron current of only  $\sim 3$  fA or  $\sim 20\,000$  electrons/s within a reasonable 10 min of integration time.

## II. EXPERIMENTAL CONCEPT

A Ti:sapphire long-cavity oscillator<sup>36</sup> provides 50-fs, 500-nJ laser pulses at a repetition rate of 5.128 MHz and a central wavelength of 800 nm, which drive all experiments in this work. Figure 1 depicts the concept of our ToF spectrometer. An electron source, consisting of a photocathode (20-nm gold layer on a sapphire substrate), a region of static acceleration to  $\sim 30$  keV of kinetic energy over a distance of 3 mm, and a solenoid for beam collimation,<sup>13</sup> generates femtosecond single-electron pulses using 266-nm laser pulses (third harmonic of the Ti:sapphire pulse train) for photoemission. These are transmitted through a diffraction or spectroscopy sample and subsequently pass through a high-voltage drift tube, discussed below. An electronic time-to-digital converter (TDC) measures the arrival time of each electron pulse at a micro-channel plate (MCP) detector with respect to a start signal, which is derived via a photodiode from the femtosecond laser pulse train. The desired high energy

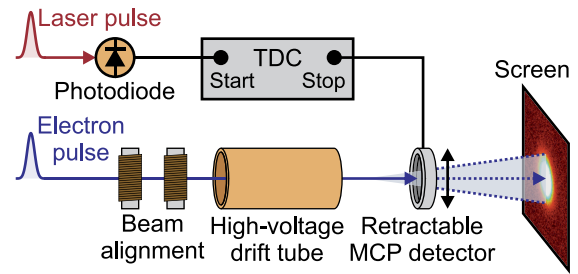


FIG. 1. Concept of the time-of-flight analyzer for femtosecond electron pulses at energies sufficient for atomic-scale diffraction (tens of keV). A time-to-digital converter (TDC) is triggered via a photodiode by a laser pulse, which is also used to generate a femtosecond electron pulse. After propagating through a high-voltage drift tube of optimized dimensions for the tens-of-keV regime, the electron pulse is detected at a micro-channel plate (MCP) detector, which stops the time measurement. A camera screen is used for beam alignment prior to time-of-flight measurements or for diffraction experiments.

resolution ( $<1$  eV FWHM at  $\sim 30$  keV of central energy) requires a large amount of temporal dispersion of the electrons inside the drift region due to the limited temporal resolution of the MCP and TDC electronics, typically on the order of 150-200 ps FWHM. To this end, the drift tube is biased nearly at the same high negative potential (about  $-30$  kV) as the photocathode for electron beam generation. The electrons are thus strongly slowed down inside the drift tube, down to only a few eV of kinetic energy for the highest resolution, thus obtaining the desired temporal dispersion. After the drift tube, they are accelerated back to the original 30-keV energy in order to facilitate detection.

The MCP detector and TDC combination used here (MCP 3636, Surface Concept GmbH) provides a digital time bin size of 27.4 ps and an impulse response of about 200 ps FWHM. The MCP stack has an active area with a diameter of 36 mm and the TDC provides a count rate of up to 7 MHz. The detector consists of four quadrants, which provide rough spatial resolution of the electron beam. In order to align the electron beam precisely along the axis of the drift tube, the MCP detector can be mechanically retracted, allowing the beam geometry to be monitored on a phosphor screen coupled to a complementary metal-oxide-semiconductor (CMOS) camera chip,<sup>37</sup> also used for recording diffraction images. Two pairs of electromagnetic deflection coils with iron cores are used in front of the drift tube for aligning the electron beam along the drift tube's symmetry axis.

Slowing down the electron pulses inside a drift tube can in principle reduce the drift velocity close to zero and hence arbitrarily enhance the energy resolution via the diverging temporal dispersion. However, this applies only to an infinitely thin and non-divergent electron beam propagating exactly along the drift tube's axis. In reality, femtosecond electron beams have a considerable diameter and divergence, given by their transverse emittance. Our gold-coated photocathode generates electron pulses with a transverse velocity spread of  $\sim 140$  km/s (rms),<sup>38</sup> corresponding to an angular spread of  $\sim 1.4$  mrad (rms) at 30 keV. In the single-electron regime, the source size is given by the laser spot diameter on the photocathode, which is on the order of a few  $\mu\text{m}$ , resulting in a transverse emittance of  $10^{-3}$ - $10^{-2}$  mm mrad (rms). The

cylindrical drift tube therefore constitutes a significant electrostatic lens; electrons entering with nonparallel momentum or at a radial distance to the axis therefore exhibit complex trajectories and differing flight times at the same kinetic energy. This geometry-related spectral broadening imposes a significant limit to the achievable energy resolution for femtosecond electron beams. This needs to be considered in the design.

### III. DESIGN AND SIMULATIONS

Generally, a longer drift tube provides more temporal dispersion, but the available space, lensing effects, and magnetic fields impose some upper limits in practice. Here, we limited the length to 200 mm due to space restrictions. In order to determine the optimum diameter of such a drift tube, we performed particle tracking simulations using finite-element methods in the non-relativistic, single-electron limit (no space charge). We found that electrostatic lensing becomes weaker for a larger diameter; on the other hand, the electric potential inside the drift tube is more homogeneous for a smaller diameter. The simulations reveal an optimum diameter of 40 mm (see the Appendix).

Figure 2(a) shows a cross section (black). The drift tube (inner cylinder) is biased at  $-30\,000$  V, while the casing (outer cylinder) is grounded. The calculated electric potential (color-coded) is approximately homogeneous inside the drift tube. A lensing effect is evident as curvature of the electric potential at the front and back openings of the drift tube. The dimensions of the grounded structure minimize these inhomogeneities,

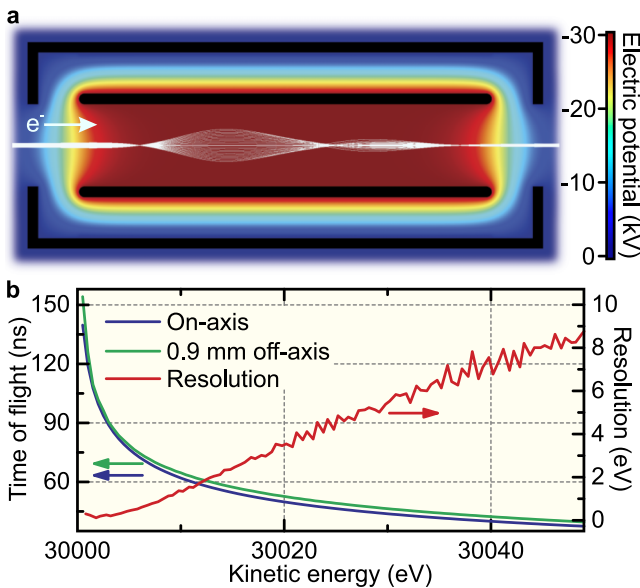


FIG. 2. Drift tube design and simulation results. (a) Cylindrically symmetric cross section through the geometry, showing the drift tube (black, inner cylinder), biased at  $-30$  kV, and the grounded casing (black, outer cylinder). The resulting electric potential is color-coded. Simulated electron trajectories for a collimated electron beam with a diameter of 1.9 mm at a kinetic energy of 30 002 eV are shown as the white traces. (b) Simulated flight times for an on-axis electron trajectory (blue) and an off-axis trajectory displaced by 0.9 mm at the entrance of the drift tube (green) as a function of kinetic energy. The resulting predicted energy resolution (red) is calculated according to Eq. (1).

while complying with the practical constraints of the design. Particle trajectories (white) are depicted for the example of a collimated monoenergetic electron beam with a diameter of 1.9 mm at a kinetic energy of 30 002 eV. The drift velocity in this example is about 840 km/s, thus an energy difference of 0.1 eV leads to a difference in time-of-flight of about 5.7 ns, which is well within the temporal resolution of the MCP detector.

The simulated flight time as a function of the electron kinetic energy  $E$  is shown in Fig. 2(b) for the on-axis trajectory (blue) and for a trajectory starting 0.9 mm off-axis at the entrance of the drift tube (green), representing the outer trajectories in Fig. 2(a). The two time-of-flight curves differ roughly by an offset of 2 ns and diverge for kinetic energies approaching the potential energy of the drift tube (30 000 eV), referred to as the threshold energy  $E_{th}$ . In order to predict our drift tube's energy resolution from the simulations, we invoke a simplified model considering the off-axis trajectory in Fig. 2(b) as the effective boundary of the distribution of trajectories within a realistic electron beam, while the on-axis trajectory represents the beam's center. The temporal dispersion per unit of energy bandwidth is given by the derivative of the time-of-flight curves with respect to energy. Thus, the energy resolution in the simulation  $R_{sim}(E)$  is strongly energy-dependent and highest close to the threshold energy. We define it here by the difference in time-of-flight between the two trajectories at a particular energy  $E$ , convoluted with the MCP detector's temporal resolution  $\tau_{det}$  and divided by the average derivative of the two time-of-flight curves with respect to energy,

$$R_{sim}(E) = \frac{2\sqrt{(t_{off-axis}(E) - t_{on-axis}(E))^2 + \tau_{det}^2}}{\left| \frac{dt_{off-axis}(E)}{dE} + \frac{dt_{on-axis}(E)}{dE} \right|}, \quad (1)$$

with  $t_{on-axis}(E)$  and  $t_{off-axis}(E)$  the flight time of the on-axis and off-axis electron trajectories, respectively. The resolution, calculated from numerical derivatives of the time-of-flight curves and assuming  $\tau_{det} = 150$  ps FWHM, is shown in Fig. 2(b) in red. The minimum value is  $\sim 0.2$  eV over a narrow energy range of up to 3 eV above  $E_{th}$ . This curve denotes an upper limit for the instrument's resolution for a beam contained within a radius of 0.9 mm (or a diameter of 1.8 mm).

### IV. CONSTRUCTION

The drift tube cylinder at a potential of about  $-30$  kV is mounted via 20-mm thick ceramic spacers inside a grounded (0 V) casing cylinder, ensuring that static electric fields do not exceed 1.5 kV/mm, which is below the limit for vacuum breakdown. The drift tube cylinder is mechanically polished and the edges are rounded with a radius of 2.5 mm in order to minimize local field enhancements. We chose copper as the material for the drift tube, since it is well suitable for optional electro-polishing, which might be required to go to even higher electron kinetic energies in future experiments. A high-voltage connection to the drift tube cylinder is provided via a thin (2 mm diameter) metal rod through a 40-mm-diameter hole

in the side of the casing cylinder. The drift tube's casing is shielded by  $\sim 1$  mm of high-permeability metal alloy ( $\mu$ -metal), providing a nearly magnetic-field-free region inside the drift tube.

## V. ALIGNMENT

For the precise alignment of the electron beam along the axis of the drift tube, the electrostatic lensing effect is utilized to monitor the beam's shape and position on the camera screen while gradually increasing the negative voltage applied to the drift tube. As the drift tube potential approaches the electron energy, distinct ring features caused by electrostatic lensing become apparent on the screen. The alignment procedure is guided by continuously improving the symmetry of the ring features and centering them, using the two pairs of electromagnetic deflection coils. The second pair of steering coils has a higher impact on the ring feature's symmetry, while the first one has a higher impact on centering. At optimum alignment, the beam spot on the camera is symmetric and its central position does not change with the drift tube potential. After alignment, the MCP detector is inserted into the beam and ToF spectra can be recorded.

In the experiment, we operate the drift tube at  $-29\,513$  V, i.e.,  $E_{\text{th}} \approx 29\,513$  eV, which allows the femtosecond electron pulses to have energies between  $E_{\text{th}}$  and  $30\,000$  eV, the maximum of the high-voltage power supply. Figure 3(a) depicts several representative ToF spectra for different kinetic energies of the electron pulses. The exposure time is about

1 s per spectrum, during which ToF events are detected at the repetition rate of the laser system, 5.1 MHz. The ToF spectra are time histograms of all measured events within the exposure time.

## VI. CALIBRATION AND CONVERSION TO ENERGY UNITS

The energy bandwidth of the single-electron pulses from our femtosecond source is  $0.2\text{--}0.3$  eV;<sup>38,39</sup> this monochromaticity of better than  $10^{-5}$  is a consequence of the single-electron emission regime without space charge broadening effects. Hence, in the ToF, the different shapes and widths of the measured spectra in Fig. 3(a) directly reveal the aforementioned geometry-related broadening effects. All spectra are rather asymmetric towards larger flight times, since electrons travel longer on any off-axis trajectory than on the limiting on-axis trajectory.

Converting the measured ToF spectrum into an energy spectrum requires a calibration. To this end, we recorded our monochromatic single-electron beam while scanning the kinetic energy of the electrons at the source. The raw ToF spectra of this calibration scan, some of which are also depicted in Fig. 3(a), are shown in Fig. 3(b) with color-coded counts on a logarithmic scale. Asymmetric geometry-related broadening around the peak is evident as a broad background at larger flight times, as discussed above.

The flight time at the peak of the ToF spectrum as a function of the kinetic energy then yields a time-energy calibration curve (dashed black line in Fig. 3(b)). Neglecting trajectory distributions, relativistic effects and non-instantaneous acceleration/deceleration inside the drift tube, the relation between the flight time after passing the drift tube  $t(E)$  and kinetic energy  $E$  follows from the classical equation of motion,

$$t(E) = d \sqrt{\frac{m_e}{2(E - E_{\text{th}})}} + t_{\text{offset}}, \quad (2)$$

with  $d$  the drift tube's length and  $m_e$  the electron's mass.  $E_{\text{th}}$  is the threshold energy below which electrons are rejected and do not pass the drift tube;  $t_{\text{offset}}$  is a time offset accounting for the flight time outside the drift tube and signal delays inside the cables and TDC.  $t_{\text{offset}}$  does not depend on the kinetic energy within the temporal resolution of the detector. Eq. (2) is only valid for a uniform motion and does not take into account the acceleration within regions of inhomogeneous electric potential. Therefore Eq. (2) only approximately reproduces the measured or simulated  $t(E)$  curves. However, we found that an empirical relation, based on a generalization of Eq. (2), can very well reproduce the actual energy dependence of the flight time,

$$t(E) = \frac{A}{(E - E_{\text{th}})^B} + t_{\text{offset}}, \quad (3)$$

with  $A$  and  $0 < B < 1$  fitting parameters.  $B$  is found to be  $\sim 0.3$  in order to reproduce the data, while it is  $0.5$  in Eq. (2). Fitting Eq. (3) to the data yields the dashed black line in Fig. 3(b), which is in excellent agreement with the

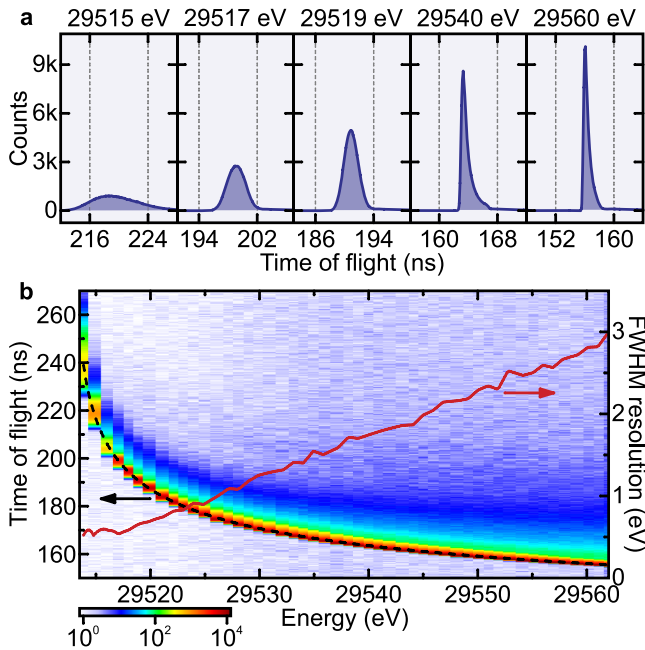


FIG. 3. Experimental calibration of the time-of-flight analyzer. (a) Representative time-of-flight spectra of a close-to-monoenergetic pulsed single-electron beam at different kinetic energies for  $E_{\text{th}} = 29\,513$  eV. (b) Calibration scan over a range of kinetic energies of  $\sim 50$  eV. The detector counts are color-coded on a logarithmic scale. The dashed black curve shows a fit through the time-of-flight peaks as a function of kinetic energy according to Eq. (3). The resulting energy resolution (red) is calculated via Eq. (4) and below  $0.6$  eV (FWHM) around the threshold energy.

numerically determined peak positions of each measured ToF spectrum.

In order to conserve the number of differential counts in such a conversion, we also need to weight the amplitude values of the spectrum by  $dt(E)/dE$ . This accounts for the nonlinear relation between the equidistantly sampled time bins of the ToF/TDC measurement and corresponding non-equidistant energy bins of the energy spectrum according to Eq. (3). We also must take into account that the transmission through the drift tube is energy-dependent and changes from  $\sim 50\%$  within a few-eV range above  $E_{th}$  to more than 90% at kinetic energies of 5 eV above  $E_{th}$  and higher. This energy-dependent efficiency is revealed in the calibration scan (Fig. 3(b)) by integrating the entire ToF spectrum for each kinetic energy value, since the source's electron flux is highly constant.<sup>37</sup>

## VII. RESOLUTION

The instrument's energy resolution in dependence on electron energy,  $R_{inst}(E)$ , can be determined, in analogy to the definition for the trajectory simulations in Eq. (1), from the derivative of the measured  $t(E)$  curve with respect to energy while considering the geometry-related energy-dependent width of each ToF spectrum in the calibration measurement,  $\tau_{cal}(E)$ . We obtain

$$R_{inst}(E) = \tau_{cal}(E) \left| \frac{dt(E)}{dE} \right|^{-1}. \quad (4)$$

Since the experimental ToF spectra are somewhat asymmetric, their width (FWHM) is determined numerically

(search for half-maximum amplitude around the peak). The result of Eq. (4) is shown in Fig. 3(b) in red. We obtain  $<0.6$  eV resolution (FWHM) over a range of up to 5 eV above  $E_{th}$  and  $<3$  eV resolution (FWHM) up to 50 eV above  $E_{th}$ . Very close to  $E_{th}$ , the measured minimum energy resolution is  $\sim 0.55$  eV (FWHM), corresponding to a relative resolution of about  $2 \times 10^{-5}$ . This is probably limited by the bandwidth of the electron pulses, which is on the same order, 0.2-0.3 eV.<sup>38,39</sup> Assuming addition in quadrature and a bandwidth of 0.3 eV, the pure instrument resolution is  $\sim 0.46$  eV.

## VIII. APPLICATION I: ULTRASHORT ELECTRON PULSE METROLOGY

Next we report some example applications. The first case is electron pulse metrology. Temporal characterization of highly-energetic electron pulses for ultrafast diffraction and microscopy has so far relied on transverse deflection methods, namely, streak cameras<sup>17,40,41</sup> and ponderomotive scattering.<sup>42-44</sup> An alternative technique, laser-cycle streaking in the energy domain, is capable of attosecond resolution<sup>33</sup> and also reveals almost the complete time-energy phase space of the electron pulse, i.e., duration, bandwidth, chirp, and longitudinal coherence. Figure 4(a) illustrates the principle: 800-nm, 50-fs (FWHM) laser pulses are reflected off a 50-nm free-standing aluminum foil, while a portion of the electron beam at  $E_0 = 25$  keV passes through ( $\sim 3.5\%$  transmission). Longitudinal optical field components perpendicular to the foil (green arrows) accelerate/decelerate the electrons as they pass through the laser focus. Since the optical field is abruptly shielded by the foil within a fraction of an optical

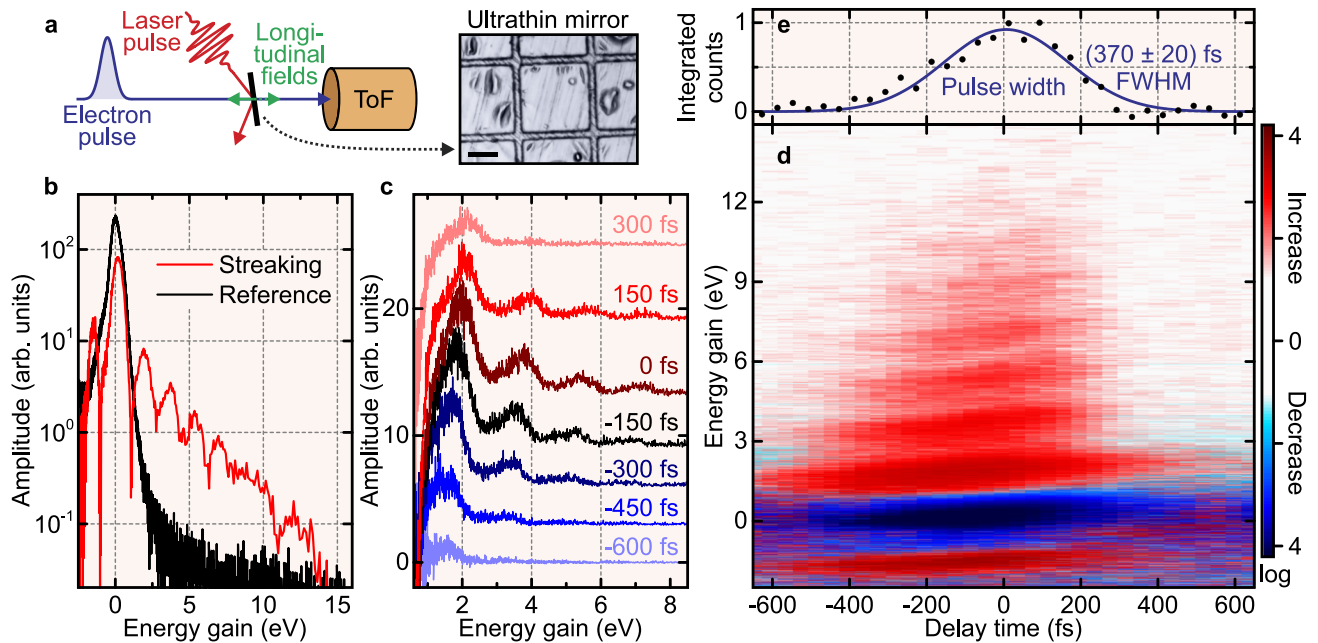


FIG. 4. Electron pulse characterization via laser streaking. (a) Experimental concept.<sup>33</sup> An electron pulse passes through a 50-nm thin aluminum foil (black scale bar, 100  $\mu\text{m}$ ) while a laser pulse is reflected off the foil. The resulting longitudinal electric field modulates the electron pulse's kinetic energy as a function of the laser-electron delay time. (b) Energy spectrum of electrons transmitted through the foil without the streaking laser (black) and at the maximum temporal overlap between electron and laser pulse (red). Energy gain is defined with respect to the central kinetic energy of 25 keV. (c) Representative streaked electron spectra at different delay times with the reference spectrum from (b) subtracted and vertically displaced for clarity. A spectral modulation with a period of  $\sim 1.6$  eV, corresponding to the streaking laser's photon energy, appears. (d) Complete streaking spectrogram with the reference subtracted; increase and decrease in detector counts are shown on logarithmic color scales. (e) Temporal cross section of the spectrogram (dots), integrated from 8 to 16 eV of energy gain, revealing an electron pulse duration of  $370 \pm 20$  fs FWHM (solid line, Gaussian fit).

cycle ( $\sim 80$  as), the electrons retain the kinetic energy gained or lost in the optical field before entering the foil. Velocity matching between the laser and electron pulse fronts along the foil's surface is achieved by choosing appropriate non-collinear angles.<sup>33</sup>

Essential for the success of this method is the time-of-flight energy analyzer. Here we report a re-measurement of the experiment described before<sup>33</sup> with emphasis on the details of detection and excellently confirm the previous results. Femtosecond electron pulses are generated as described above and collimated with a well-aligned<sup>45</sup> magnetic lens to a beam diameter of about  $100 \mu\text{m}$ . ToF spectra of the laser-streaked electrons are recorded as a function of the delay between electron and laser pulses and converted to energy using a previous calibration measurement according to Eq. (3) and applying the appropriate weighting. The integration time is about 15 s per spectrum at a laser repetition rate of  $\sim 100$  kHz and about one electron per pulse. The energy loss region, i.e., the part of the streaked electron spectrum below 25 keV, suffers from off-axis trajectories of the unstreaked electrons, an effect that is absent in the gain region. Therefore, the threshold energy of the drift tube,  $E_{\text{th}}$ , is set to 3 eV below  $E_0$ , which essentially rejects the energy loss part of the streaking spectrum and matches the window of highest energy resolution to the gain region close to the central energy. This choice is optimum for determining electron coherence properties via quantum interference;<sup>33</sup> both the energy loss and the energy gain region exhibit identical features in the case of cycle-averaged laser streaking.

Fig. 4(b) shows a reference electron spectrum (black) without a streaking laser and a streaked spectrum at the optimum temporal overlap (red). It is evident that electron counts are redistributed from the central peak to higher and lower energies by the streaking field into sidebands with a period of  $\sim 1.6$  eV, corresponding to the streaking pulse's photon energy. The time-of-flight analyzer's resolution is clearly sufficient to observe this quantum-mechanical interference of single-electron wave packets with themselves.<sup>46</sup> Note that the visibility of the interference features decreases at higher energies (see also Fig. 4(d)), owing to the ToF analyzer's energy-dependent decrease of resolution. High-energy streaking sidebands could be observed via a change of  $E_{\text{th}}$  in the analyzer.

Fig. 4(c) shows streaked spectra at different delay times between the electron and streaking laser pulses. The reference spectrum is subtracted from all streaked spectra, emphasizing the changes, and the spectra are vertically displaced for clarity. Two effects are observed with increasing delay time: an appearance and disappearance of sidebands with temporal overlap and a continuous shift of the interference features towards higher energies. This becomes clearer when depicting all streaking spectra (with the reference subtracted) as a spectrogram,<sup>33</sup> as shown in Fig. 4(d), displaying both the increase and decrease in counts on logarithmic scales as a function of delay time and energy gain. Here the extremely high throughput efficiency of the ToF spectrometer proves invaluable for detecting count changes over 4 orders of magnitude in the dynamic range. The tilt of the interference

features reveals the electron pulse's correlation between energy and time, i.e., its chirp. We measure  $\sim 1.1$  eV/ps with higher-energetic components arriving earlier, confirming the earlier results (1.1 eV/ps).<sup>33</sup> The temporal profile of the spectrogram at highest gain or loss reveals the electron pulse shape in time. In the experiment, we find this convergence of the cross-correlation towards the electron pulse profile at energy gain values above  $\sim 8$  eV in good agreement with the previous experiment.<sup>33</sup> Figure 4(e) shows the spectrogram integrated between 8 eV and 16 eV of energy gain (an upper limit for noise rejection), yielding the electron pulse's profile in time. The electron pulse's duration is  $370 \pm 20$  fs (FWHM), in good agreement with the  $360 \pm 20$  fs measured before.<sup>33</sup> Interestingly, there might be a small temporal asymmetry in the evaluated electron pulse profile, which could originate from a non-Gaussian electron momentum distribution at the source,<sup>38</sup> but we do not feel this significant enough to analyze here in detail.

Overall, this experiment is a confirmation of the previous results. The time-of-flight analyzer provides sufficient efficiency and resolution for laser streaking at electron energies of tens of keV. Thanks to the analyzer's high throughput, a streaking experiment takes only about 8 min, allowing an almost online adjustment of electron pulse parameters for minimizing chirp and duration.<sup>47</sup> The analyzer is also helpful for finding time-zero with few-femtosecond precision<sup>35</sup> and for confirming the experiment's temporal response function independently of the dynamics to be investigated.

## IX. APPLICATION II: HIGH-RESOLUTION LASER-MICROWAVE PHASE DETECTOR

Precise synchronization between a femtosecond laser pulse train and a microwave signal is a key requirement for electron pulse compression via time-dependent microwave fields.<sup>16,17,24,47,48</sup> Imperfect synchronization introduces timing jitter and thus limits the achievable temporal resolution of pump-probe experiments. Here we show how the ToF energy analyzer can be used as an *in situ* electron-microwave delay detector with few-femtosecond precision. The concept was reported before<sup>24</sup> and is based on precisely recording the energy change of electron pulses after passing through a microwave compressor. The analyzer's energy resolution and detection efficiency directly translate to precision and measurement speed, respectively, and the time-of-flight detector is therefore ideal.

Figure 5(a) depicts the experiment: A  $\text{TM}_{010}$  cavity with a resonance frequency of 6.237 GHz and a bandwidth of  $\sim 2$  MHz<sup>24</sup> is inserted into the electron beam and fed by a microwave signal which is derived from the 1216<sup>th</sup> harmonic of the laser's repetition rate via optically enhanced photodetection<sup>34</sup> and amplified to about 2 W. The same laser pulse train is used for electron pulse generation as described above. The  $\text{TM}_{010}$  mode exhibits an on-axis electric field, which accelerates or decelerates the passing electron pulses in dependence on time, causing the electron pulse to compress at one of the zero crossings of the microwave's phase.

For small phase changes around the zero-crossing phase, the overall energy change of the electron beam is

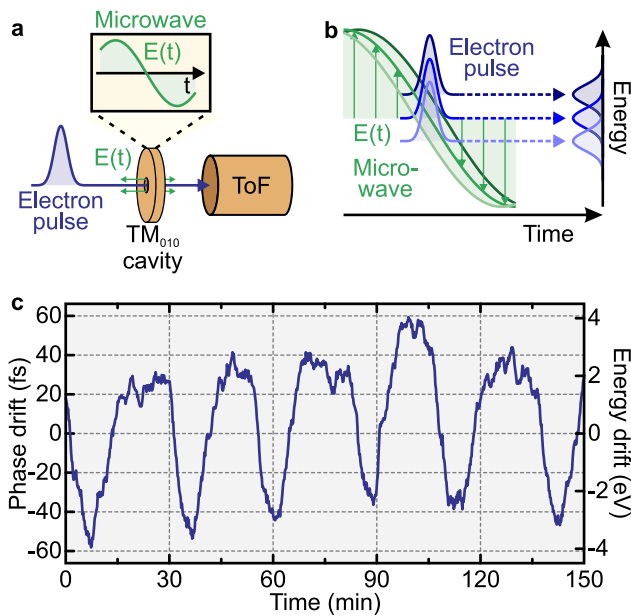


FIG. 5. Concept of a laser-microwave phase detector based on the time-of-flight analyzer. (a) A microwave cavity with a  $TM_{010}$  mode at 6.237 GHz is driven by a microwave signal that is directly derived from the same laser pulse train also used to generate femtosecond electron pulses.<sup>34,35</sup> The electron pulse's kinetic energy is recorded by the ToF analyzer after passing through the cavity. (b) Depending on the microwave's phase inside the cavity, electrons gain or lose energy, which is the principle of a streak camera in the energy domain (see text). The relationship between delay and energy shift is approximately linear around the microwave's zero-crossing, here 69 eV/ps. (c) Long-term phase (or timing) drift of the microwave recorded with the ToF analyzer by monitoring the drift of the electron pulse's central kinetic energy after passing the cavity. The pronounced half-hour oscillations reflect the temperature fluctuations in the laboratory and can be compensated.<sup>35</sup> The accuracy of the phase detector is about 1 fs (rms) for 5 s of integration time at 5.1 MHz repetition rate.

proportional to the microwave's phase (see Fig. 5(b)). This constitutes a streak camera in the energy domain<sup>24</sup> capable of determining the microwave phase *in situ*,<sup>48</sup> i.e., directly via the same electron beam also used for pump-probe diffraction/spectroscopy. Approximately, the coefficient between microwave phase delay and electron energy is linear and can be determined experimentally,<sup>24,47,49</sup> we obtain  $69 \pm 2$  eV/ps in our experiment. The ToF analyzer is operated at a threshold energy of  $\sim 30$  eV below the kinetic energy of the electrons (25 keV), in order to cover the electron beam's increased energy bandwidth of  $\sim 26$  eV FWHM after compression, via  $(370 \pm 20 \text{ fs}) \times (69 \pm 2 \text{ eV/ps})$ . Time-of-flight spectra are acquired with an integration time of 5 s at a count rate of about  $2 \times 10^5 \text{ s}^{-1}$  and converted to energy as described above. The energy peak is determined by Gaussian fits and the result plotted in Fig. 5(c) in dependence on time over several hours. A timing drift with a half-hour period and roughly 100 fs peak-to-peak amplitude reflects a periodic temperature drift in the laboratory due to imperfections of the cooling system on that day. On a time scale of minutes, the timing drift is on the order of a few fs (rms). Thanks to the time-of-flight analyzer's high resolution, the upper limit of the measurement accuracy is about 1 fs (rms) for a 5 s integration time, given by the statistical noise of the data. This corresponds to a phase resolution of about  $40 \mu\text{rad}$  (rms) at a microwave frequency of 6.237 GHz. The long-term

energy drift of the ToF analyzer alone, determined with the microwave compressor switched off, is on the order of 0.1 eV over many hours, corresponding to a long-term systematic error of  $\sim 1.5$  fs (or  $\sim 60 \mu\text{rad}$ ) when used as a phase detector. Thus, the drift measured in Fig. 5(c) is entirely attributed to timing/phase drift between the microwave inside the cavity and the electrons.

Since the ToF analyzer provides data for almost every single electron passing the compressor cavity (50%-90%), it can also be applied for jitter analysis at much higher frequencies, of course at the expense of reduced statistics in determining the peak energy and thus the time. In principle, however, it is possible to apply a time-of-flight analyzer like the one reported here as an *in situ* electron-microwave phase detector providing few-fs precision.<sup>35</sup>

## X. APPLICATION III: TIME-RESOLVED EELS

Another potential application for our high-resolution ToF energy analyzer is the emerging field of time-resolved electron energy loss spectroscopy<sup>11,12</sup> for probing site-specific structural dynamics of a material via its plasmonic or core-loss resonances. The ToF analyzer presented in this work can be used as a compact and inexpensive alternative to energy-filtering electron microscopes when imaging is not required. Also, the device's relaxed demands on electron beam quality allow applying the substantially shorter electron pulse durations achievable from work-function-matched sources<sup>38,39</sup> or after microwave compression, where beam emittance is substantially worse as compared to electron microscopy.

In order to demonstrate the applicability of our ToF spectrometer for time-resolved electron energy loss spectroscopy, we report here a pump-probe measurement on a 50-nm free-standing aluminum foil, see Fig. 6. The electron pulses are generated as described above, with 0.2-0.3 eV bandwidth at 25 keV. The pump laser pulse parameters are essentially identical to the laser streaking experiment described above, but with the laser incident at  $30^\circ$  and the electric field parallel to the sample surface. This geometry is chosen in order to suppress the laser streaking effect (see above) by destructive optical interference at the foil surface. The kinetic energy of the incoming electrons is set to 25 015 eV, while the drift tube's threshold energy,  $E_{\text{th}}$ , is set 20 eV lower in order to cover the range of aluminum's bulk plasmon resonance at high resolution. ToF spectra are recorded as a function of the delay between laser and electron pulses at a count rate of about  $2 \times 10^4 \text{ s}^{-1}$  and converted to energy as described above. A shutter in the laser beam path is used to acquire a reference (non-pumped) spectrum for every delay step, as reported before.<sup>12</sup> Thus, only the difference between pumped and non-pumped spectra is recorded.

A static EELS spectrum from the aluminum foil is shown in the inset of Fig. 6, depicting the characteristic plasmon loss peak of bulk aluminum at about 16 eV, as well as the zero-loss peak (ZLP). Note that the width and shape of both peaks are dominated by aberrations inside the drift tube. For example, the ZLP is wider than the plasmon loss peak due to the ToF analyzer's energy-dependent resolution.

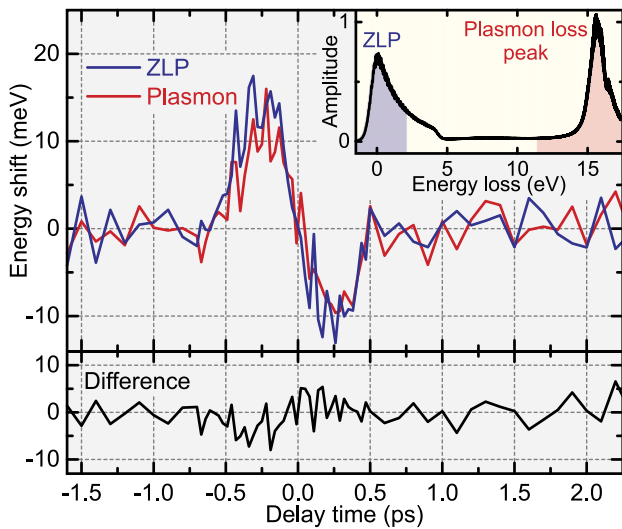


FIG. 6. Time-resolved electron energy loss spectroscopy (EELS) of aluminum using 800-nm laser pump pulses. The inset shows a static EELS spectrum (10 s of integration time at 5.1 MHz repetition rate) with the bulk plasmon resonance at about 16 eV of loss. Each pump-probe delay step is integrated for 10 min ( $\sim 1.2 \times 10^7$  electron counts). The zero-loss peak (ZLP, blue) and the plasmon loss peak (red) both experience an energy shift of about  $\pm 10$  meV around time-zero, which is attributed to the streaking effect<sup>33</sup> caused by residual longitudinal laser fields at imperfect polarization (see text). No relative shift of the plasmon loss peak with respect to the ZLP (black) is visible, yielding an upper limit for laser-induced intraband changes of aluminum's plasma frequency given by the accuracy of the analyzer of  $\sim 3$  meV (rms) in determining the time-dependent energy position of an EELS peak.

Despite lacking the ability to accurately resolve sub-peak features, the ToF analyzer is well capable of determining the spectral position of a peak with high accuracy via Gaussian fits. The blue curve in Fig. 6 shows the change of the ZLP position as a function of the pump-probe delay. Here, a positive energy shift means less energy loss in the context of EELS. Each delay step is integrated for 400 s (a total of  $\sim 8 \times 10^6$  electron counts) for a pumped spectrum and for 200 s ( $\sim 4 \times 10^6$  electron counts) for a non-pumped reference spectrum. A small up/down energy shift by roughly  $\pm 10$  meV around time-zero is visible. This is attributed to residual laser streaking by longitudinal electric fields potentially originating from imperfect linear polarization or roughness of the aluminum foil. The energy modulation by laser streaking is asymmetric in time due to the electron pulse's chirp and a corresponding center shift with pump-probe delay (compare Figs. 4(c) and 4(d)). The temporal width of the feature ( $\sim 0.4$  ps peak-to-peak) resembles the pump-probe cross-correlation width previously determined by laser streaking ( $\sim 370$  fs). The plasmon loss peak (red curve in Fig. 6) exhibits an almost identical energy shift around time-zero. This is expected because plasmonic energy loss seemingly occurs on a time scale significantly shorter than the propagation time through the foil (80 as); both ZLP electrons and plasmon loss electrons appear to experience exactly the same optical streaking effect in the laser field cycles. Interesting in this context would be such an experiment with attosecond electron pulses,<sup>50,51</sup> as recently proposed.<sup>52</sup> The ToF analyzer could be instrumental for such an endeavor.

Figure 6 (bottom) also shows the difference between the energy shift of the ZLP and the plasmon loss peak. This measurement allows to assign an accuracy of  $\sim 3$  meV (rms) for detecting the position of an EELS peak, given by the standard deviation of the difference trace (black curve) outside of the region of temporal overlap ( $< -0.5$  ps and  $> 0.5$  ps). No net energy shift is observable, indicating that laser-induced intraband changes of aluminum's plasma frequency at our experimental conditions are too small to be resolved even with this instrument. Nevertheless, this measurement demonstrates that energy shifts of about 5 meV are detectable, confirming the excellent performance of the ToF analyzer for future femtosecond EELS experiments.

## XI. SUMMARY AND CONCLUSIONS

These examples show the general applicability of a ToF analyzer in the regime of electron energies around 30 keV. Key benefits over other approaches are the high throughput efficiency for quite imperfect electron beams and the remarkably good resolution in the sub-eV range. We conceive no conceptual limitation in scaling up the device to even higher electron energies via increasing the separation between drift tube and the grounded support structures. Realistic femtosecond electron beams, as common in ultrafast electron diffraction, can be analyzed without any signal-reducing apertures. These capabilities allow for a wide range of applications, three of which have been demonstrated in this work (optical streak camera, laser-microwave phase detector, time-resolved EELS). The compact and linear beam path of the ToF analyzer renders it especially useful for integration with femtosecond electron diffraction apparatuses, advancing their capabilities into the energy domain and providing a versatile tool for electron pulse metrology, pump-probe timing diagnostics and time-resolved spectroscopy.

## ACKNOWLEDGMENTS

This work was supported by the Munich-Centre for Advanced Photonics and the European Research Council. We thank Ferenc Krausz for generous support and Soo Hoon Chew for fruitful discussions regarding energy conversion and the suggestion of a suitable MCP detector.

## APPENDIX: OPTIMIZING THE RADIUS OF THE DRIFT TUBE

In order to determine the optimum radius of the drift tube for a given length, particle tracking simulations were performed as a function of the drift tube's radius for electron trajectories that are displaced parallel to the drift tube's axis (modeling the beam's diameter) or at an angle to the axis (modeling the beam's divergence). High energy resolution is achievable for a wide range of drift tube radii. However, the maximum acceptable beam diameter and divergence for a desired energy resolution are found to have a pronounced dependence on the drift tube geometry. Given the 200-mm length, there is an optimum radius for which the largest beam

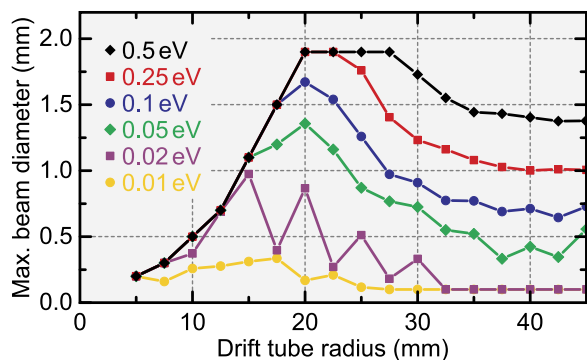


FIG. 7. Optimization of the drift tube's radius from particle tracking simulations. The maximum acceptable electron beam diameter is shown as a function of the drift tube's radius for different specified energy resolutions between 0.01 eV and 0.5 eV. An optimum radius is evident for each specified resolution, which maximizes the acceptable beam diameter (see text). Note that the curves are clipped at 1.9 mm, since simulations were only performed for beam diameters up to this value.

diameter and divergence are acceptable. This constitutes the optimum trade-off between trajectory distortions due to electrostatic lensing (less for larger radius) and homogeneity of the potential inside the drift tube (better for smaller radius).

The curves in Fig. 7 denote maximum beam diameters, for which a specified energy resolution, between 0.01 eV and 0.5 eV, is achievable. An optimum radius of the drift tube is evident for all curves and a slight shift of the optimum radius towards higher values is visible for worse (i.e., larger) specified resolutions. Note that the beam diameter is clipped in the simulations at 1.9 mm, since the trajectories are only simulated up to this value, covering all practical beam diameters. It is crucial to design the drift tube with the optimum radius for the desired resolution, since this significantly relaxes the quality of the electron beam required. A 20 mm radius of the drift tube was chosen for the experiment, which is optimized for a resolution of 0.1 eV, allowing a beam diameter of up to 1.7 mm, well above the typical beam diameters in femtosecond diffraction (limited usually by sub-mm sample dimensions). The achievable energy resolution is found to scale in a similar way with the electron beam's divergence (at a fixed beam diameter) as with its diameter (at a fixed divergence); hence the optimum drift tube radius for maximizing the acceptable beam diameter also maximizes the acceptable divergence. For a resolution of 0.1 eV and a drift tube radius of 20 mm, the maximum acceptable divergence is about 4 mrad, assuming an infinitely thin beam. Since a realistic beam has both a finite diameter and divergence, the maximum acceptable beam diameter for a specified resolution is reduced if a finite divergence is present. For example, according to the simulation, a beam diameter of 1 mm allows for a maximum divergence of about 2.4 mrad in order to achieve an energy resolution of 0.1 eV.

atomic motions in the optical suppression of charge density waves," *Nature* **468**(7325), 799–802 (2010).

- <sup>3</sup>D. J. Flannigan and A. H. Zewail, "4D electron microscopy: Principles and applications," *Acc. Chem. Res.* **45**(10), 1828–1839 (2012).
- <sup>4</sup>M. Gao, C. Lu, H. Jean-Ruel, L. C. Liu, A. Marx, K. Onda, S. Koshihara, Y. Nakano, X. Shao, T. Hiramatsu, G. Saito, H. Yamochi, R. R. Cooney, G. Moriena, G. Sciaini, and R. J. D. Miller, "Mapping molecular motions leading to charge delocalization with ultrabright electrons," *Nature* **496**(7445), 343–346 (2013).
- <sup>5</sup>C. Gerbig, A. Senftleben, S. Morgenstern, C. Sarpe, and T. Baumert, "Spatio-temporal resolution studies on a highly compact ultrafast electron diffractometer," *New J. Phys.* **17**, 043050 (2015).
- <sup>6</sup>H. Ihee, V. A. Lobastov, U. M. Gomez, B. M. Goodson, R. Srinivasan, C. Y. Ruan, and A. H. Zewail, "Direct imaging of transient molecular structures with ultrafast diffraction," *Science* **291**(5503), 458–462 (2001).
- <sup>7</sup>V. R. Morrison, R. P. Chatelain, K. L. Tiwari, A. Hendaoui, A. Bruhacs, M. Chaker, and B. J. Siwick, "A photoinduced metal-like phase of monoclinic VO<sub>2</sub> revealed by ultrafast electron diffraction," *Science* **346**(6208), 445–448 (2014).
- <sup>8</sup>G. Sciaini and R. J. D. Miller, "Femtosecond electron diffraction: heralding the era of atomically resolved dynamics," *Rep. Prog. Phys.* **74**(9), 096101 (2011).
- <sup>9</sup>H.-C. Shao and A. F. Starace, "Detecting electron motion in atoms and molecules," *Phys. Rev. Lett.* **105**(26), 263201 (2010).
- <sup>10</sup>G. M. Vanacore, J. Hu, W. Liang, S. Bietti, S. Sanguinetti, and A. H. Zewail, "Diffraction of quantum dots reveals nanoscale ultrafast energy localization," *Nano Lett.* **14**(11), 6148–6154 (2014).
- <sup>11</sup>F. Carbone, O.-H. Kwon, and A. H. Zewail, "Dynamics of chemical bonding mapped by energy-resolved 4D electron microscopy," *Science* **325**(5937), 181–184 (2009).
- <sup>12</sup>R. M. van der Veen, T. J. Penfold, and A. H. Zewail, "Ultrafast core-loss spectroscopy in four-dimensional electron microscopy," *Struct. Dyn.* **2**(2), 024302 (2015).
- <sup>13</sup>S. Lahme, C. Kealhofer, F. Krausz, and P. Baum, "Femtosecond single-electron diffraction," *Struct. Dyn.* **1**(3), 034303 (2014).
- <sup>14</sup>R. J. D. Miller, "Femtosecond crystallography with ultrabright electrons and x-rays: Capturing chemistry in action," *Science* **343**(6175), 1108–1116 (2014).
- <sup>15</sup>B. J. Siwick, J. R. Dwyer, R. E. Jordan, and R. J. D. Miller, "Ultrafast electron optics: Propagation dynamics of femtosecond electron packets," *J. Appl. Phys.* **92**(3), 1643–1648 (2002).
- <sup>16</sup>E. Fill, L. Veisz, A. Apolonski, and F. Krausz, "Sub-fs electron pulses for ultrafast electron diffraction," *New J. Phys.* **8**, 272 (2006).
- <sup>17</sup>T. van Oudheusden, P. L. E. M. Pasmans, S. B. van der Geer, M. J. de Loos, M. J. van der Wiel, and O. J. Luiten, "Compression of subrelativistic space-charge-dominated electron bunches for single-shot femtosecond electron diffraction," *Phys. Rev. Lett.* **105**(26), 264801 (2010).
- <sup>18</sup>A. Gubbens, M. Barfels, C. Trevor, R. Twesten, P. Mooney, P. Thomas, N. Menon, B. Kraus, C. Mao, and B. McGinn, "The GIF quantum, a next generation post-column imaging energy filter," *Ultramicroscopy* **110**(8), 962–970 (2010).
- <sup>19</sup>M. Mukai, J. S. Kim, K. Omoto, H. Sawada, A. Kimura, A. Ikeda, J. Zhou, T. Kaneyama, N. P. Young, J. H. Warner, P. D. Nellist, and A. I. Kirkland, "The development of a 200 kV monochromated field emission electron source," *Ultramicroscopy* **140**, 37–43 (2014).
- <sup>20</sup>J. Rubio-Zuazo, M. Escher, M. Merkel, and G. R. Castro, "High voltage-cylinder sector analyzer 300/15: A cylindrical sector analyzer for electron kinetic energies up to 15 keV," *Rev. Sci. Instrum.* **81**(4), 043304 (2010).
- <sup>21</sup>M. Sowinska, T. Bertaud, D. Walczyk, S. Thiess, M. A. Schubert, M. Lukosius, W. Drube, C. Walczyk, and T. Schroeder, "Hard x-ray photoelectron spectroscopy study of the electroforming in Ti/HfO<sub>2</sub>-based resistive switching structures," *Appl. Phys. Lett.* **100**(23), 233509 (2012).
- <sup>22</sup>Y. Takata, M. Yabashi, K. Tamasaku, Y. Nishino, D. Miwa, T. Ishikawa, E. Ikenaga, K. Horiba, S. Shin, M. Arita, K. Shimada, H. Namatame, M. Taniguchi, H. Nohira, T. Hattori, S. Södergren, B. Wannberg, and K. Kobayashi, "Development of hard X-ray photoelectron spectroscopy at BL29XU in SPring-8," *Nuclear Instruments and Methods in Physics Nucl. Instrum. Methods Phys. Res., Sect. A* **547**(1), 50–55 (2005).
- <sup>23</sup>P. Torelli, M. Sacchi, G. Cautero, M. Cautero, B. Krastanov, P. Lacovig, P. Pittana, R. Sergo, R. Tommasini, A. Fondacaro, F. Offi, G. Paolicelli, G. Stefani, M. Grioni, R. Verbeni, G. Monaco, and G. Panaccione, "Experimental setup for high energy photoemission using synchrotron radiation," *Rev. Sci. Instrum.* **76**(2), 023909 (2005).

<sup>1</sup>P. Baum, D. S. Yang, and A. H. Zewail, "4D visualization of transitional structures in phase transformations by electron diffraction," *Science* **318**(5851), 788–792 (2007).

<sup>2</sup>M. Eichberger, H. Schafer, M. Krumova, M. Beyer, J. Demsar, H. Berger, G. Moriena, G. Sciaini, and R. J. D. Miller, "Snapshots of cooperative

- <sup>24</sup>A. Gliserin, A. Apolonski, F. Krausz, and P. Baum, "Compression of single-electron pulses with a microwave cavity," *New J. Phys.* **14**, 073055 (2012).
- <sup>25</sup>D. P. Hale and W. D. Allen, "An electrostatic electron energy analyzer for 3-20 keV electrons," *J. Phys. E: Sci. Instrum.* **4**(4), 311 (1971).
- <sup>26</sup>H. F. Wellenstein, "Simple recording Möllenstedt electron-velocity analyzer," *J. Appl. Phys.* **44**(8), 3669–3674 (1973).
- <sup>27</sup>C. A. Arrell, J. Ojeda, M. Sabbar, W. A. Okell, T. Witting, T. Siegel, Z. Diveki, S. Hutchinson, L. Gallmann, U. Keller, F. van Mourik, R. T. Chapman, C. Cacho, N. Rodrigues, I. C. E. Turcu, J. W. G. Tisch, E. Springate, J. P. Marangos, and M. Chergui, "A simple electron time-of-flight spectrometer for ultrafast vacuum ultraviolet photoelectron spectroscopy of liquid solutions," *Rev. Sci. Instrum.* **85**(10), 103117 (2014).
- <sup>28</sup>R. E. Kennerly, "High-resolution pulsed electron beam time-of-flight spectrometer," *Rev. Sci. Instrum.* **48**(12), 1682–1688 (1977).
- <sup>29</sup>G. Lebedev, A. Tremsin, O. Siegmund, Y. Chen, Z.-X. Shen, and Z. Hussain, "Complete momentum and energy resolved TOF electron spectrometer for time-resolved photoemission spectroscopy," *Nucl. Instrum. Methods Phys. Res., Sect. A* **582**(1), 168–171 (2007).
- <sup>30</sup>J. Lin, N. Weber, A. Wirth, S. H. Chew, M. Escher, M. Merkel, M. F. Kling, M. I. Stockman, F. Krausz, and U. Kleineberg, "Time of flight-photoemission electron microscope for ultrahigh spatiotemporal probing of nanoplasmonic optical fields," *J. Phys.: Condens. Matter* **21**(31), 314005 (2009).
- <sup>31</sup>A. Kothe, J. Metje, M. Wilke, A. Moguevski, N. Engel, R. Al-Obaidi, C. Richter, R. Golnak, I. Y. Kiyani, and E. F. Aziz, "Time-of-flight electron spectrometer for a broad range of kinetic energies," *Rev. Sci. Instrum.* **84**(2), 023106 (2013).
- <sup>32</sup>G. F. Mancini, B. Mansart, S. Pagano, B. van der Geer, M. de Loos, and F. Carbone, "Design and implementation of a flexible beamline for fs electron diffraction experiments," *Nucl. Instrum. Methods Phys. Res., Sect. A* **691**, 113–122 (2012).
- <sup>33</sup>F. O. Kirchner, A. Gliserin, F. Krausz, and P. Baum, "Laser streaking of free electrons at 25 keV," *Nat. Photonics* **8**(1), 52–57 (2014).
- <sup>34</sup>A. Gliserin, M. Walbran, and P. Baum, "Passive optical enhancement of laser-microwave synchronization," *Appl. Phys. Lett.* **103**(3), 031113 (2013).
- <sup>35</sup>M. Walbran, A. Gliserin, K. Jung, J. Kim, and P. Baum, "5-fs laser-electron synchronization for pump-probe crystallography and diffraction," *Phys. Rev. Appl.* **4**, 044013 (2015).
- <sup>36</sup>S. Naumov, A. Fernandez, R. Graf, P. Dombi, F. Krausz, and A. Apolonski, "Approaching the microjoule frontier with femtosecond laser oscillators," *New J. Phys.* **7**, 216 (2005).
- <sup>37</sup>C. Kealhofer, S. Lahme, T. Urban, and P. Baum, "Signal-to-noise in femtosecond electron diffraction," *Ultramicroscopy* **159**(Part 1), 19–25 (2015).
- <sup>38</sup>M. Aidelsburger, F. O. Kirchner, F. Krausz, and P. Baum, "Single-electron pulses for ultrafast diffraction," *Proc. Natl. Acad. Sci. U. S. A.* **107**(46), 19714–19719 (2010).
- <sup>39</sup>L. Kasmi, D. Kreier, M. Bradler, E. Riedle, and P. Baum, "Femtosecond single-electron pulses generated by two-photon photoemission close to the work function," *New J. Phys.* **17**, 033008 (2015).
- <sup>40</sup>M. Gao, Y. Jiang, G. H. Kassier, and R. J. D. Miller, "Single shot time stamping of ultrabright radio frequency compressed electron pulses," *Appl. Phys. Lett.* **103**(3), 033503 (2013).
- <sup>41</sup>G. H. Kassier, K. Haupt, N. Erasmus, E. G. Rohwer, H. M. von Bergmann, H. Schwoerer, S. M. M. Coelho, and F. D. Auret, "A compact streak camera for 150 fs time resolved measurement of bright pulses in ultrafast electron diffraction," *Rev. Sci. Instrum.* **81**(10), 105103 (2010).
- <sup>42</sup>M. Gao, H. Jean-Ruel, R. R. Cooney, J. Stampe, M. de Jong, M. Harb, G. Sciaini, G. Moriena, and R. J. D. Miller, "Full characterization of RF compressed femtosecond electron pulses using ponderomotive scattering," *Opt. Express* **20**(11), 12048–12058 (2012).
- <sup>43</sup>C. T. Hebeisen, R. Ernstorfer, M. Harb, T. Dartigalongue, R. E. Jordan, and R. J. D. Miller, "Femtosecond electron pulse characterization using laser ponderomotive scattering," *Opt. Lett.* **31**(23), 3517–3519 (2006).
- <sup>44</sup>V. R. Morrison, R. P. Chatelain, C. Godbout, and B. J. Siwick, "Direct optical measurements of the evolving spatio-temporal charge density in ultrashort electron pulses," *Opt. Express* **21**(1), 21–29 (2013).
- <sup>45</sup>D. Kreier, D. Sabonis, and P. Baum, "Alignment of magnetic solenoid lenses for minimizing temporal distortions," *J. Opt.* **16**(7), 075201 (2014).
- <sup>46</sup>P. Reckenthaeler, M. Centurion, V. S. Yakovlev, M. Lezius, F. Krausz, and E. E. Fill, "Proposed method for measuring the duration of electron pulses by attosecond streaking," *Phys. Rev. A* **77**(4), 042902 (2008).
- <sup>47</sup>A. Gliserin, M. Walbran, F. Krausz, and P. Baum, "Sub-phonon-period compression of electron pulses for atomic diffraction," *Nat. Commun.* **6**, 8723 (2015).
- <sup>48</sup>G. J. H. Brussaard, A. Lassise, P. L. E. M. Pasmans, P. H. A. Mutsaers, M. J. van der Wiel, and O. J. Luiten, "Direct measurement of synchronization between femtosecond laser pulses and a 3 GHz radio frequency electric field inside a resonant cavity," *Appl. Phys. Lett.* **103**(14), 141105 (2013).
- <sup>49</sup>P. L. E. M. Pasmans, G. B. van den Ham, S. F. P. Dal Conte, S. B. van der Geer, and O. J. Luiten, "Microwave TM<sub>010</sub> cavities as versatile 4D electron optical elements," *Ultramicroscopy* **127**, 19–24 (2013).
- <sup>50</sup>P. Baum, "Towards ultimate temporal and spatial resolutions with ultrafast single-electron diffraction," *J. Phys. B: At., Mol. Opt. Phys.* **47**(12), 124005 (2014).
- <sup>51</sup>A. Feist, K. E. Echternkamp, J. Schauss, S. V. Yalunin, S. Schafer, and C. Ropers, "Quantum coherent optical phase modulation in an ultrafast transmission electron microscope," *Nature* **521**(7551), 200–203 (2015).
- <sup>52</sup>N. Talebi, W. Sigle, R. Vogelgesang, and P. van Aken, "Numerical simulations of interference effects in photon-assisted electron energy-loss spectroscopy," *New J. Phys.* **15**(5), 053013 (2013).